Bowtie Limited Diffraction Beams for Low-Sidelobe and Large Depth of Field Imaging

Jian-yu Lu, *Member, IEEE*

***Abstract*—Limited diffraction beams such as Bessel beams and X waves have a large depth of field and thus could have many applications. However, these beams have higher sidelobes as compared to conventional focused beams in their focal planes. In this paper, a new class of limited diffraction beams is developed. These beams are termed bowtie limited diffraction beams because they have bowtie shapes in a plane perpendicular to the beam axis. To obtain pulse-echo images of low sidelobes and a large depth of field, a bowtie limited diffraction beam is used in transmission and its 90° rotated response (around the beam axis) is used in reception. Unlike the summation-subtraction method developed previously, this method does not reduce image frame rate or dynamic range of signals and is not motion sensitive. The theory of the bowtie limited diffraction beams is developed. Computer simulation of the theoretical beams under practical conditions, such as finite aperture, finite bandwidth, and causal excitation, is performed with the Rayleigh-Sommerfeld diffraction formula. The simulated beams are very close to those predicted analytically over a large depth of field.**

I. Introduction

In 1983, Brittingham discovered a localized wave solution to the free-space scalar wave equation in electromagnetics that he termed "focus wave modes" [1]. This wave remains focused over a large distance with only local deformation as it propagates. The focus wave modes were further developed by Ziolkowski [2] and many other investigators [3]–[10]. Independent of Brittingham and Ziolkowski's work, in 1987 Durnin discovered the first limited diffraction beam [11]. Unlike localized waves, in theory, limited diffraction beams can propagate to infinite distance without changing their sharply focused beam shapes. Durnin has termed the new beams "nondiffracting beams" [11] or "diffraction-free beams" [12]. Because Durnin's terminologies are controversial in scientific communities, the new term "limited diffraction beams" has been used on the basis that all practical beams will diffract eventually [13], [14]. Durnin's beams (called also Bessel beams because their lateral beam profiles are a Bessel function) have been further studied in both optics [15]–[17] and acoustics [18]–[20]. Theoretically, limited diffraction beams can only be produced with an infinite aperture. In practice, these beams can be closely approximated with a finite aperture over a large depth of field. Because of this property, limited diffraction beams could have applications in medical imaging [21]–[24], tissue characterization [25], nondestructive evaluation of materials [26], and Doppler velocity estimation [27], as well as in optics [28] and electromagnetics [7], [29], [30].

Recently, a new type of limited diffraction beams was discovered [31]–[33]. These beams were called X waves because they have an X-like shape in a plane along their propagation axis. X waves are different from Bessel beams because they are nondispersive in isotropic/homogeneous media. Like Bessel beams, X waves have a large depth of field and could have many applications [21], [34]–[39]. The discussion of advantages and trade-offs of Bessel beams and X waves as compared to conventional focused beams can be found in a review paper [13].

Although limited diffraction beams have a large depth of field, they have higher sidelobes as compared to conventional focused beams in their focal plane. Localized waves may achieve lower sidelobes, but they demand an impractical transducer bandwidth [13], [40]. High sidelobes may lower contrast in medical imaging [41], [42] and make it difficult to detect low scattering objects such as small cysts. High sidelobes also increase the effective sampling volume, which lowers the image resolution in tissue characterization [25].

High sidelobes are not unique with limited diffraction beams. They also occur with methods that increase the depth of field of conventional beams, such as using a ring aperture [43]–[45] or the Axicon [46]–[48]. Efforts have been made to reduce sidelobes. For example, Burckhardt *et al.* [49] have divided a ring transducer into eight equal segments and arranged the segments into two orthogonal groups. One group was used to transmit and the other to receive. Then, the whole geometry was rotated around the axis of the ring by, say 45°, to repeat the process, and the resulting RF signals were summed. This method reduces the sidelobes of the ring to some extent but the image frame rate is reduced by a factor of two. Macovski and Norton [50] have weighted a ring transducer with the powers of the cosine and sine functions to transmit and receive, respectively. This resulted in sidelobe reductions in two orthogonal directions of the ring, but leaves high sidelobes in other directions. Moshfeghi [51] and Macovski *et al.* [50] used the idea of transmitting and receiving with different aperture sizes. However, this method does not reduce the sidelobes significantly. Recently, a summation-subtraction method has been developed to reduce the sidelobes of the pulse-echo responses of limited diffraction beams [14], [52]. This method is similar to those used by Wild

Manuscript received January 2, 1995; revised July 7, 1995. This work was supported in part by Grants CA 54212 and CA 43920 from the National Institutes of Health.

The author is with the Biodynamics Research Unit, Department of Physiology and Biophysics, Mayo Clinic and Foundation, Rochester, MN 55905 USA.

IEEE Log Number 9415104.

[43] and Burckhardt *et al*. [44] for a ring aperture and that used by Patterson *et al*. [53] for an Axicon transducer. The problems with the summation-subtraction method are that it is sensitive to object motion, the final signals have a small dynamic range due to the subtraction of larger signals, and the process requires multiple transmissions that lower image frame rate leading to blurred images of moving objects such as the heart. Other methods for reducing the sidelobes of limited diffraction beams, such as deconvolution [54], dynamic focused reception, etc., have also been suggested and they are reviewed in [13, pp. 417–422].

In this paper, another new type of limited diffraction beams is developed. These beams are called bowtie limited diffraction beams because they have a bowtie shape in a plane perpendicular to their propagation axis. They are obtained from spatial derivatives of the limited diffraction beams studied previously (such as the X waves and the Bessel beams) in one transverse direction (in the bowtie plane). In theory, these beams also have an infinite depth of field. Even if produced with a finite aperture, they have the same very large depth of field as the original limited diffraction beams. The difference between bowtie limited diffraction beams and the original beams is that the sidelobes of the former has a strong angle dependency. The sidelobes are the highest and the same as those of original limited diffraction beams in the direction of derivatives where they are proportional to $1/r^{1/2}$ as $r \to \infty$, and where r is the radial distance from the beam axis, and the lowest in the direction perpendicular to that of the derivatives. Because of the angle dependency, pulse-echo systems that have both low sidelobes and large depth of field can be constructed by transmitting with a bowtie limited diffraction beam and receiving with its response rotated 90° around the beam axis. The advantages of this method for sidelobe reduction are that it does not reduce the dynamic range of the received signals, nor the image frame rate. The rotation of the bowtie limited diffraction beams or their responses could be achieved by electronic switching of radiator elements or using a 90° interlaced bowtie radiator that has a shape of the Maltese cross-processor previously reported for speckle reduction [55].

In the following, the theory of the bowtie limited diffraction beams will be developed. Then, the beams will be simulated under practical conditions, such as finite aperture, finite bandwidth, and causal excitation, of a radiator with the Rayleigh-Sommerfeld diffraction formula. Finally, there is a brief discussion and a conclusion.

II. Theory of Bowtie Limited Diffraction Beams

In this section, bowtie limited diffraction beams that are exact solutions to the isotropic-homogeneous scalar wave equation will first be derived. Then, a few examples of these beams will be given and their applications in pulse-echo systems for low-sidelobe imaging will be demonstrated.

A. Bowtie Limited Diffraction Beams

To derive bowtie limited diffraction beams, it is necessary to review the previously studied X waves [31]–[33] and Bessel beams [11], [31]. A three-dimensional (3-D) isotropic/homogeneous scalar wave equation in cylindrical coordinates is given by

$$\left[\frac{1}{r}\frac{\partial}{\partial r}\left(r\frac{\partial}{\partial r}\right)+\frac{1}{r^2}\frac{\partial^2}{\partial \phi^2}+\frac{\partial^2}{\partial z^2}-\frac{1}{c^2}\frac{\partial^2}{\partial t^2}\right]\Phi=0, \quad (1)$$

where $r=\sqrt{x^2+y^2}$ is radial distance, $\phi=\tan^{-1}(y/x)$ is azimuthal angle, z is the axial axis that is perpendicular to the plane defined by r and ϕ, t is time, c is the speed of sound or light, and Φ represents acoustic pressure or the Hertz potential that is a function of $r,\ \phi,\ z,$ and t. From (1), one obtains X waves [31]–[33]

$$\Phi_{X_n}(r,\phi,z-c_1t)= e^{in\phi}\int_0^\infty B(k)J_n(kr\sin\zeta)e^{-k[a_0-i(z\cos\zeta-ct)]}dk, \quad (n=0,\ 1,\ 2,...) \quad (2)$$

and Bessel beams [11], [31]

$$\Phi_{J_n}(r,\phi,z-c_1t)=AJ_n(\alpha r)e^{i(\beta z-\omega t+n\phi)}, \quad (n=0,\ 1,\ 2,\ ...), \quad (3)$$

where the subscripts "X" and "J" represent X waves and Bessel beams, respectively, n is a nonnegative integer, c_1 is phase velocity ($c_1=c/\cos\zeta$ for X waves and $c_1=\omega/\beta$ for Bessel beams), where ω is angular frequency, ζ is an Axicon angle [56] that is a constant for a given X wave, and $\beta=\sqrt{k^2-\alpha^2}$ is the propagation constant of Bessel beams, where $k=\omega/c$ is wavenumber and α is a scaling factor that controls the lateral resolution (or main beamwidth) of Bessel beams, A is a complex constant, $J_n(\cdot)$ is the nth-order Bessel function of the first kind, a_0 is a constant that determines the decay speed of the high-frequency components of X waves, and $B(k)$ is any well-behaved function of k and could represent the transfer functions of practical radiators (antennas or acoustic transducers). The X waves (2) and the Bessel beams (3) are exact solutions to the wave equation (1). They are limited diffraction beams because they are explicit functions of the propagation term, $z-c_1t$. If $z-c_1t=$ const. (traveling with the waves), Φ_{X_n} and Φ_{J_n} are not functions of z and t. This means that Φ_{X_n} and Φ_{J_n} in (2) and (3) represent waves that will propagate to infinite distance without changing their wave shapes.

Taking derivatives of the X waves and the Bessel beams in (2) and (3), respectively, in one transverse direction, say, y, we obtain the bowtie limited diffraction beams

$$\frac{\partial^m}{\partial y^m}\Phi_{X_n}(r,\phi,z-c_1t) \quad (4)$$

and

$$\frac{\partial^m}{\partial y^m}\Phi_{J_n}(r,\phi,z-c_1t), \quad (5)$$

where m is a nonnegative integer and is the order of the derivatives. These new beams are exact solutions to the wave equation (1) (in addition, any linear combinations of derivatives of waves in rectangular coordinates are also solutions to

(1)) and they are still limited diffraction beams because the propagation term, $z - c_1 t$, is retained after the derivatives.

From (2) and (3), we see that the Bessel beams are a special case of the X waves (or monochromatic X waves). If $B(k) = \delta(k - k_0)$, where $k_0 = \omega_0/c$ and ω_0 is a constant angular frequency, (2) is given by

$$\Phi_{X_n}(r, \phi, z - c_1 t) = e^{in\phi} J_n(k_0 r \sin\zeta) e^{-k_0[a_0 - i(z\cos\zeta - ct)]}, \quad (n = 0, 1, 2, ...). \tag{6}$$

Let $\alpha = k_0 \sin\zeta$, $\beta = \sqrt{k_0^2 - \alpha^2} = k_0 \cos\zeta$, and $A = e^{-k_0 a_0}$, (6) is identical to (3). For this reason, in the following, we consider primarily the bowtie X waves. The properties of the bowtie Bessel beams are expected to be similar to those of the bowtie X waves (Appendix B).

B. Examples

Two examples will be given below showing the properties of the bowtie limited diffraction beams.

The integration in (2) can be evaluated if $B(k) = a_0$ [31]

$$\Phi_{XBB_n} = \frac{a_0 (r\sin\zeta)^n e^{in\phi}}{\sqrt{M}\left(\tau + \sqrt{M}\right)^n} \quad , \quad (n = 0, 1, 2, ...), \tag{7}$$

where the subscript "BB" means broadband, Φ_{XBB_n} represents an nth-order broadband X wave,

$$M = (r\sin\zeta)^2 + \tau^2, \tag{8}$$

and where

$$\tau = [a_0 - i(z\cos\zeta - ct)]. \tag{9}$$

Because for $n > 0$ the field patterns of Φ_{XBB_n} are complicated, in the following, only the cases where $n = 0$ will be considered. With $n = 0$, (7) is simplified and becomes rotary symmetric (independent of ϕ), and represents the zeroth-order X wave [31]

$$\Phi_{XBB_0} = \frac{a_0}{\sqrt{(r\sin\zeta)^2 + [a_0 - i(zcos\zeta - ct)]^2}}. \tag{10}$$

Substitute (10) into (4) and let $m = 4$ and $m = 10$ (these two orders of derivatives are chosen to demonstrate the trend of the bowtie beams of increasing orders), we obtain

$$\Phi_{X_{B4}} = a_{X_{B4}} \cdot 3a_0 \sin^4\zeta \frac{35y^4 \sin^4\zeta - 30y^2 M \sin^2\zeta + 3M^2}{M^{9/2}} \tag{11}$$

and (12), shown at the bottom of the page, respectively, where $\Phi_{X_{Bm}}$ represents the mth-derivative bowtie X wave, and $a_{X_{B4}} = a_0^4/\left(9\sin^4\zeta\right)$ and $a_{X_{B10}} = -a_0^{10}/\left(893025\sin^{10}\zeta\right)$ are constants that normalize the peak of the bowtie X waves to one. In obtaining these constants, we assume that there is only one peak for both (11) and (12), and the peaks appear at $x = 0$, $y = 0$, and $z = c_1 t$, i.e., $\lim\limits_{x\to 0}\left\{\lim\limits_{y\to 0}\left\{\lim\limits_{z\to c_1 t}\{\Phi_{X_{Bm}}\}\right\}\right\} = \max\limits_{\forall \vec{r}, t}\{\Phi_{X_{Bm}}\} = 1$. Equations (11) and (12) can be verified by directly inserting them into (1).

The 4th and 10th derivative bowtie X waves ((11) and (12)) are shown in Fig. 1. For comparison, the zeroth-order X wave (10) is also shown. The transfer function, $B(\omega/c)$, in (2) is applied to both the bowtie and the zeroth-order X waves, and is assumed to be a Blackman window function [57]

$$B\left(\frac{\omega}{c}\right) = \begin{cases} 0.42 - 0.5\cos\frac{\pi\omega}{\omega_0} + 0.08\cos\frac{2\pi\omega}{\omega_0}, & 0 \le \omega \le 2\omega_0 \\ 0, & \text{otherwise,} \end{cases} \tag{13}$$

where $\omega_0 = 2\pi f_0$, and $f_0 = 2.5$ MHz is the central frequency (the -6-dB relative bandwidth of (13) is about 81%, or, the bandwidth is equal to $0.81 \times f_0$). The parameter, a_0, for the bowtie X waves and the zeroth-order X wave is chosen so that the bandwidths of the waves are determined mainly by (13). From Fig. 1, it is seen that the bowtie waves are strongly angle dependent and their ties become thinner as the order of derivative increases.

C. Asymptotic Behaviors of Bowtie Limited Diffraction Beams

To understand the energy distribution of the bowtie limited diffraction beams in space, we need to know the asymptotic behaviors of the bowtie X waves given in (11) and (12) (Appendix A)

$$|\Phi_{X_{B4}}| \underset{r\to\infty}{\sim} \frac{b_1 \sin^4\phi}{r^{1/2}} + O\left(\frac{1}{r^{1/2}}\right)\sin^2\phi + \frac{d_1}{r^{(4+1)/2}} \tag{14}$$

and

$$|\Phi_{X_{B10}}| \underset{r\to\infty}{\sim} \frac{b_1 \sin^{10}\phi}{r^{1/2}} + O\left(\frac{1}{r^{1/2}}\right)\sin^2\phi + \frac{d_1}{r^{(10+1)/2}}, \tag{15}$$

where "$\sim$" means "similar to," "$O(\cdot)$" represents the terms that approach zero faster than the function inside the bracket as $r \to \infty$, and b_1 and d_1 are a set of constants that may have different values for (14) and (15).

It is seen from (14) and (15) that the asymptotic behaviors of the bowtie X waves are angle dependent. This is different

$$\Phi_{X_{B10}} = a_{X_{B10}} \cdot 14175 a_0 \sin^{10}\zeta \times \left\{\frac{46189y^{10}\sin^{10}\zeta - 109395y^8 M\sin^8\zeta + 90090y^6 M^2\sin^6\zeta}{M^{21/2}} + \frac{-30030y^4 M^3\sin^4\zeta + 3465y^2 M^4\sin^2\zeta - 63M^5}{M^{21/2}}\right\}, \tag{12}$$

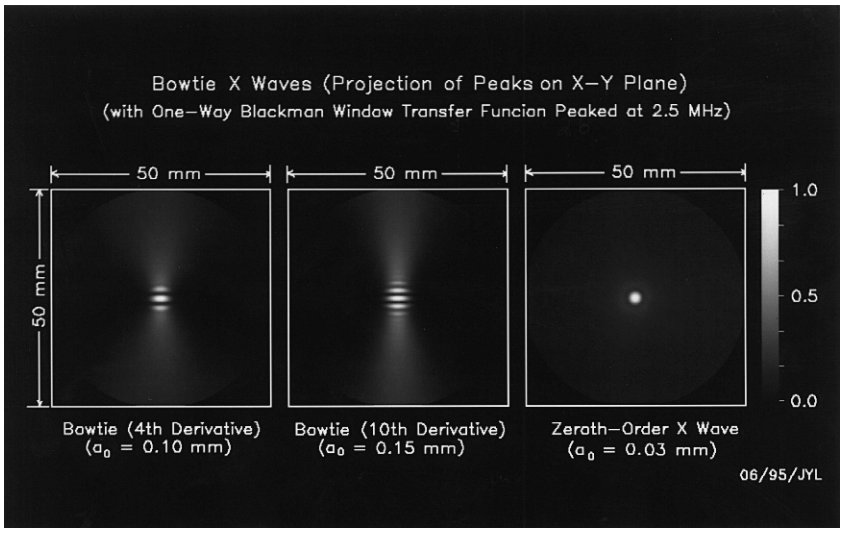

Fig. 1. The 4th (left panel) and 10th derivative (central panel) bowtie X waves, and their comparison with the zeroth-order X wave (right panel). The waves are obtained theoretically from the wave equation and filtered with a Blackman window function peaked at 2.5 MHz. The images in the panels are shown in a plane perpendicular to the wave axis and are obtained from the peaks of the absolute values of the real-part of the waves projected along the axis to the image plane. Therefore, these images give the highest sidelobes of the waves. The parameters used in this figure are as follows: the Axicon angle, ζ, of both the bowtie X waves and the zeroth-order X wave is 6.6°; the constant, a_0, that determines the fall-off speed of the high-frequency components (see (2)) of the zeroth-order X wave, the 4th and 10th derivative bowtie X waves, is 0.03 mm, 0.10 mm, and 0.15 mm, respectively; the gray-scale of the images is linear, that is ranged from 0 to 1.0 in 256 levels; and the images are in the $x - y$ plane.

from that of the zeroth-order X wave (10) whose asymptotic behavior is given by

$$|\Phi_{XBB_0}| = \left|a_0/\sqrt{M}\right| \underset{r\to\infty}{\sim} 1/r^{1/2} \tag{16}$$

(see (A2) in Appendix A). If $\phi = 0$ (perpendicular to the direction of derivatives), the fields in (14) and (15) are given by $|\Phi| \underset{r\to\infty}{\propto} 1/r^{(m+1)/2}$, where $m = 4, 10$ or other nonnegative even integers, and "$\propto$" means "proportional to." If $\phi = 90°$ (in the direction of derivatives), one always gets $|\Phi| \underset{r\to\infty}{\propto} 1/r^{1/2}$ which is the same as the X waves and the Bessel beams [31]. For $0° < \phi < 90°$, the first terms in (14) and (15) will be the dominating terms eventually as $r \to \infty$. However, because of the angular weighting, $\sin^m \phi$, this happens only for very large r if ϕ is small or m is large.

D. Sidelobe Reduction for Pulse-Echo Systems

Although rotary-symmetric limited diffraction beams, such as the zeroth-order X wave (10) and Bessel beam (3), have a large depth of field [21], [23], they have high sidelobes when applied to pulse-echo systems. To obtain pulse-echo systems that have both low sidelobes and large depth of field, bowtie limited diffraction beams can be used. This is because the sidelobes of bowtie limited diffraction beams are strongly angle dependent. To obtain low sidelobes, a bowtie limited diffraction beam is used in transmission and its 90° rotated response is in reception. The resulting pulse-echo responses of the systems are the time convolution of the transmission beam and the reception response. The pulse-echo responses of the 4th and 10th derivative bowtie X waves ((11) and (12)) and their comparison to that of the zeroth-order X wave (10) are shown in Fig. 2. Log compression is used to show the small sidelobes of the bowtie pulse-echo responses. The Blackman window function (13) is added to both transmission and reception which gives a 58% −6-dB relative bandwidth. It is seen that the sidelobes of the pulse-echo responses of bowtie beams are much lower than those of the zeroth-order X wave.

The method for reduction of sidelobes of pulse-echo systems with bowtie limited diffraction beams has several advantages as compared to the summation-subtraction method studied previously [14]. It does not subtract two large signals resulting in small differences that may have small dynamic ranges in the presence of noise. It is not sensitive to object motion because no subtraction of RF signals is involved. In addition, image frame rate is not reduced (low image frame rate may lead to blurred images of moving objects such as the heart) since no multiple transmissions are used.

To get a more quantitative view of the sidelobes of the bowtie limited diffraction pulse-echo systems, line plots of the images in Fig. 2 are given in Fig. 3. It is seen that the sidelobes of the pulse-echo responses of the bowtie X waves decrease as the order of derivative increases. The highest sidelobes of these responses appear at $\phi = 45°$ and the best lateral resolution (or the smallest first sidelobe) is around $\phi = 30°$. For comparison with the conventional focused beams at their focuses, plots of sidelobes of the pulse-echo response of a circular focused piston transducer at its focus is also shown. The beam pattern of the piston transducer at the focus is called the Airy pattern and is determined by a Jinc function [58, p. 64]

$$\text{Jinc}(\alpha_j r) = \frac{2J_1(\alpha_j r)}{\alpha_j r}, \tag{17}$$

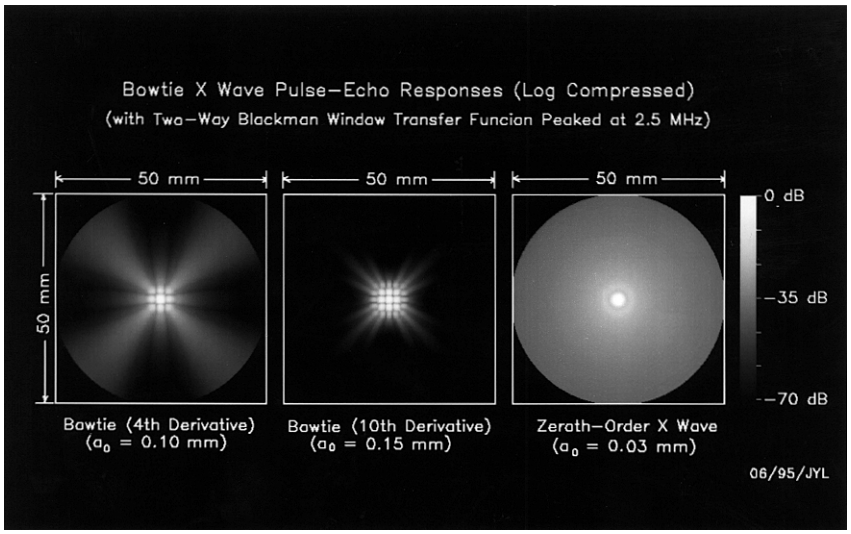

Fig. 2. This figure has the same format as that of Fig. 1 except that it shows the highest sidelobes of the pulse-echo (two-way) responses of the bowtie X waves and the zeroth-order X wave. A Blackman window function peaked at 2.5 MHz is added to both transmission and reception (two-way Blackman window). For the bowtie X waves, the reception responses are rotated 90° from the transmission waves around the propagation axis. Images in all panels are obtained from the peaks of the absolute values of the pulse-echo responses projected along the axis to the image plane. The images are log-compressed and displayed in the range from 0 dB to −70 dB with 256 gray levels. The parameters of the waves are the same as those in Fig. 1.

where r is the radial distance and α_j is a scaling factor that controls the mainlobe width of the function and is related to the f-number and the central wavelength of the beam. In Fig. 3, $\alpha_j = 1772.06\ \text{m}^{-1}$ so that the −6-dB beamwidth of the pulse-echo Jinc response is about the same as that of the zeroth-order X wave. It should be noted that although the sidelobes of the pulse–echo response of the 10th derivative bowtie X wave at $\phi = 45°$ are about 15 dB higher than those of the Airy pattern near the radial distance $r = \pm 25$ mm (see Fig. 3), they are about 15 dB lower than those of a linear array at its focus whose beam pattern is a Sinc function [58, p. 62]

$$\text{Sinc}(\alpha_s r) = \frac{\sin(\alpha_s r)}{\alpha_s r}, \tag{18}$$

where $\alpha_s = 1516.40\ \text{m}^{-1}$ is a scaling factor (with $\alpha_s = 1516.40\ \text{m}^{-1}$, the −6-dB beamwidth of the pulse-echo response of the Sinc function is the same as that of the Jinc function).

III. Realization of Bowtie Limited Diffraction Beams with Finite Aperture Radiators

The theoretical bowtie limited diffraction beams derived in the last section are exact solutions to the wave equation without boundary conditions. Therefore, they can only be produced with an infinite aperture. Because the asymptotic behaviors of the bowtie limited diffraction beams along the direction of derivatives are proportional to $1/r^{1/2}$, an infinite total energy is required. In addition, these beams are not causal, i.e., they must exist from $t = -\infty$. In this section, the bowtie limited diffraction beams will be produced approximately for practical conditions, such as, finite aperture, finite bandwidth, and causal excitation, using the Rayleigh-Sommerfeld diffraction formula [58].

A. Rayleigh-Sommerfeld Diffraction Formula

The Rayleigh-Sommerfeld diffraction formula is an integration that sums the spatially weighted contributions of the fields from baffled point sources on a radiator surface. It is given by [58]

$$\tilde{\Phi}_R(\vec{r},k) = \frac{1}{i\lambda}\int_0^{2\pi} d\phi' \int_0^{D/2} r' dr' \tilde{\Phi}_S(r',\phi',k)\frac{e^{ikr_{01}}}{r_{01}^2} z + \frac{1}{2\pi}\int_0^{2\pi} d\phi' \int_0^{D/2} r' dr' \tilde{\Phi}_S(r',\phi',k)\frac{e^{ikr_{01}}}{r_{01}^3} z, \tag{19}$$

where the first and the second terms represent the high- and low-frequency contributions, respectively, $r' - \phi'$ are the polar coordinates on the surface of the radiator, where $r' = \sqrt{x'^2 + y'^2}$ and $\phi' = \tan^{-1} y'/x'$, z is the distance on the axial axis that is perpendicular to the $r'-\phi'$ plane, $r'dr'd\phi'$ is a differential area on the surface, λ is the wavelength, r_{01} is the distance between the differential area and the spatial point, $\vec{r} = (r,\phi,z)$, where the field is to be calculated, D is the diameter of the radiator (assume a circular radiator), $\tilde{\Phi}_S(r',\phi',k)$ is an aperture weighting function (the Fourier transform (spectrum) of the beams with respect to time, t, evaluated at the surface of the radiator, $z = 0$), where the subscript "S" represents "surface of radiator," and $\tilde{\Phi}_R(\vec{r},k)$ is the Fourier transform of the beams to be calculated at the spatial point, $\vec{r}$, where the subscript "R" means "calculated by the Rayleigh-Sommerfeld diffraction formula." From $\tilde{\Phi}_R(\vec{r},k)$, we obtain the beams

$$\Phi_R(\vec{r},t) = \mathcal{F}^{-1}\left[\tilde{\Phi}_R\left(\vec{r},\frac{\omega}{c}\right)\right], \tag{20}$$

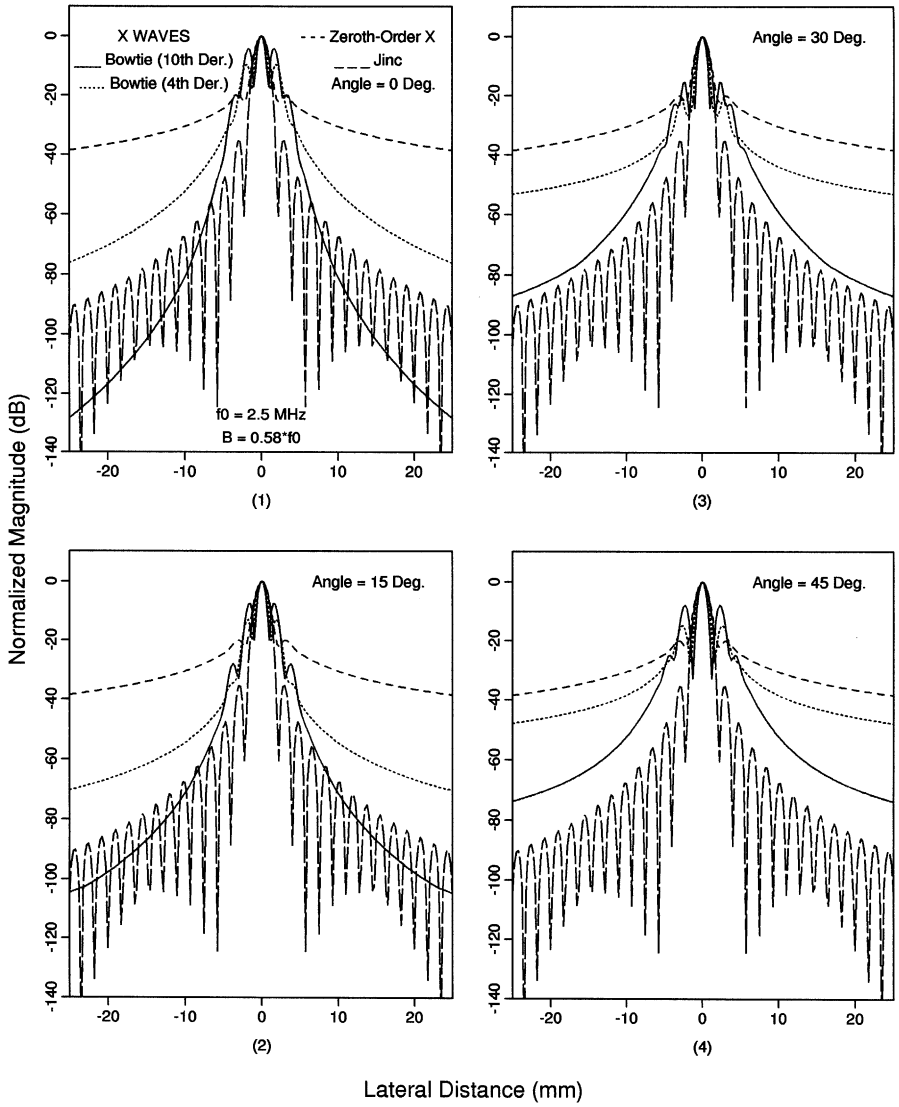

Fig. 3. Line plots of the theoretical pulse-echo responses (see Fig. 2) of the 4th (dotted lines) and 10th derivative (full lines) bowtie X waves and the zeroth-order X wave (dashed lines) at four angles: $\phi = 0°$ (Panel (1)), 15° (Panel (2)), 30° (Panel (3)), and 45° (Panel (4)) cross the axis of the beams. For comparison, the pulse-echo Jinc function or Airy pattern of a focused circular piston beam at its focus is also shown (long dashed lines). The angles $\phi = 0°$ and 90° correspond to the x and y axes, respectively (the horizontal and vertical axes of Fig. 2). The lateral axis of the plots is from -25 mm to 25 mm and the vertical is from 0 dB to -140 dB.

where $\mathcal{F}^{-1}$ represents "the inverse Fourier transform" [59] that is defined as

$$f(t) = \frac{1}{2\pi} \int_{-\infty}^{+\infty} F(\omega) e^{-i\omega t} d\omega. \tag{21}$$

The Rayleigh-Sommerfeld diffraction formula (19) has taken into account the practical conditions of a radiator, such as the finite aperture, D, and finite bandwidth (assuming that $\widetilde{\Phi}_S(r', \phi', k)$ is a band-pass function of k). The causality of the beams can be assured by truncating the beams with a rectangular time window, i.e., $|\Phi_R(\vec{r}, t)|_{\left|t - \frac{z}{c_1}\right| \geq t_0} = 0$, where t_0 is a preset constant.

B. Bowtie X Waves

To use (19), we need to obtain the spectrum of the bowtie limited diffraction beams at the surface of the radiator. Let $n = 0$ in (2) and substitute the result into (4), we have

$$\frac{\partial^m}{\partial y^m} \Phi_{X_0}(r, \phi, z - c_1 t) = \int_0^{\infty} B(k) \left[\frac{\partial^m}{\partial y^m} J_0(kr \sin\zeta) \right] e^{-k[a_0 - i(z\cos\zeta - ct)]} dk. \tag{22}$$

Compare (22) with (21), we obtain the spectrum of the bowtie X waves

$$\tilde{\Phi}_{X_{Bm}}\left(\vec{r}, \frac{\omega}{c}\right) = \frac{2\pi}{c} B\left(\frac{\omega}{c}\right) \left[\frac{\partial^m}{\partial y^m} J_0\left(\frac{\omega}{c} r \sin\zeta\right) \right] \cdot H\left(\frac{\omega}{c}\right) e^{-\frac{\omega}{c}(a_0 - iz\cos\zeta)} \tag{23}$$

where

$$H\left(\frac{\omega}{c}\right) = \begin{cases} 1 & , \quad \omega \geq 0 \\ 0 & , \quad \omega < 0 \end{cases} \tag{24}$$

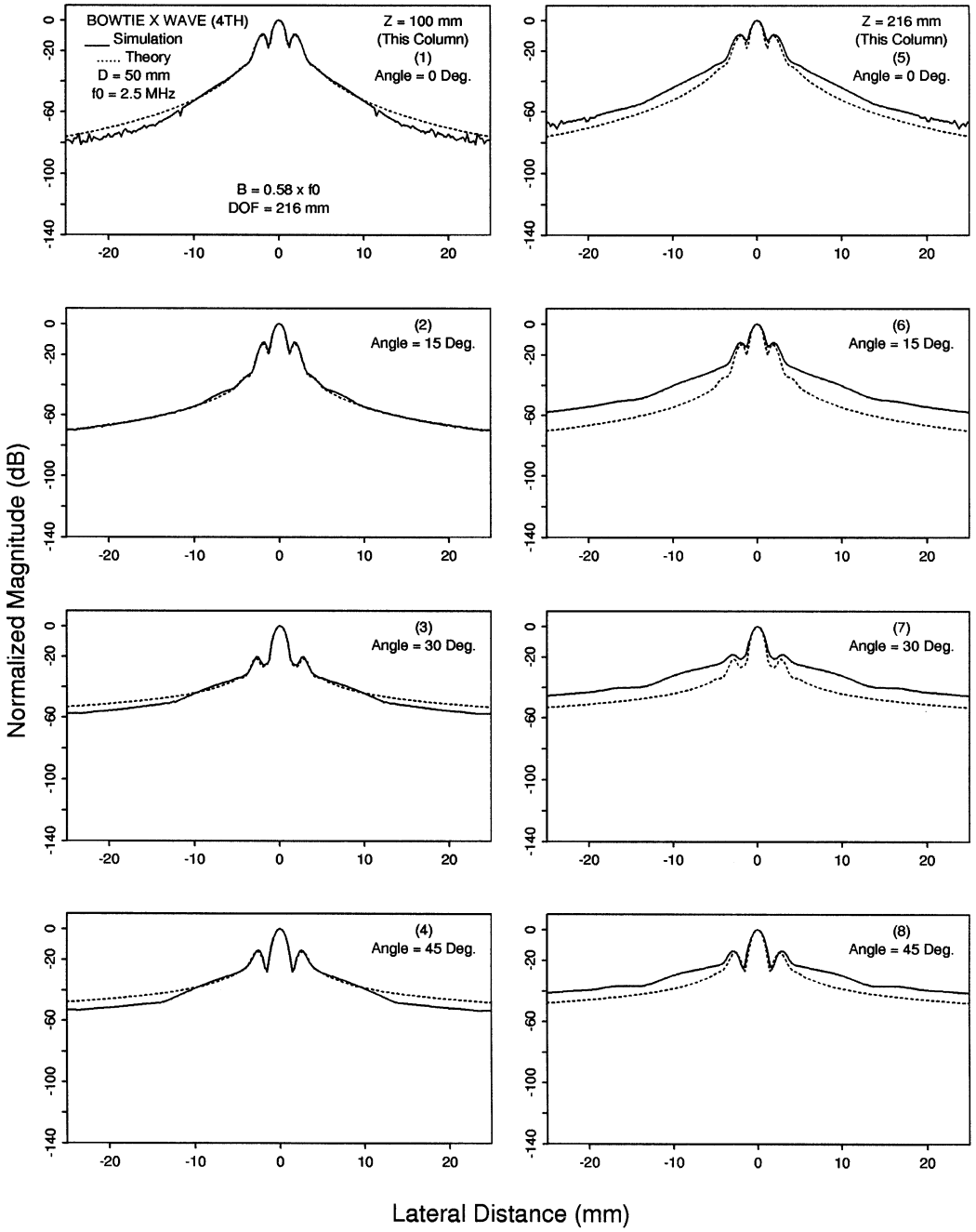

Fig. 4. Line plots of the pulse-echo (two-way) responses of the 4th derivative bowtie X wave (full lines) simulated with the Rayleigh-Sommerfeld diffraction formula at four different angles, $\phi = 0^\circ$ (first row), 15° (second row), 30° (third row), and 45° (bottom row), cross the axis of the beam, and at two axial distances, $z = 100$ mm (left column) and 216 mm (right column). For comparison, the plots of the theoretical pulse-echo responses of the 4th derivative bowtie X wave are copied from Fig. 3 (dotted lines). The parameters of the simulated beam are the same as those of the theoretical beam in Figs. 2 and 3 except that the diameter of the radiator is 50 mm instead of infinity. With this diameter, the depth of field of the beam is about 216 mm.

is the Heaviside step function [59]. At the surface of a radiator, $z = 0$, we obtain from (23)

$$\tilde{\Phi}_{SX}\left(r', \phi', \frac{\omega}{c}\right) = \frac{2\pi}{c} B\left(\frac{\omega}{c}\right)\left[\frac{\partial^m}{\partial y'^m} J\left(\frac{\omega}{c} r' \sin\zeta\right)\right] \cdot H\left(\frac{\omega}{c}\right) e^{-\frac{\omega}{c} a_0} \tag{25}$$

where $y' = r' \sin\phi'$. The derivatives of the Bessel function in (25) are tedious. Examples of the derivatives with $m = 4$ and 10, and their relationship to the bowtie Bessel beams are given in Appendix B.

Replacing $\widetilde{\Phi}_S(r', \phi', k)$ in (19) with (25) and using (20), we obtain approximated (simulated) 4th (Fig. 4) and 10th derivative (Fig. 5) bowtie X waves. The parameters used in the simulation are the same as those used in the theoretical beams (Figs. 1–3). Because

$$|\Phi_R(\vec{r}, t)|_{\left|t - \frac{z}{c_1}\right| > t_0} << \max_{\forall \vec{r}, t} |\Phi_R(\vec{r}, t)|, \tag{26}$$

where $t_0 = 8.33\ \mu$s, the simulated bowtie X waves are truncated with a moving rectangular window to produce causal waves. The diameter of the radiator for the simulated beams is 50 mm.

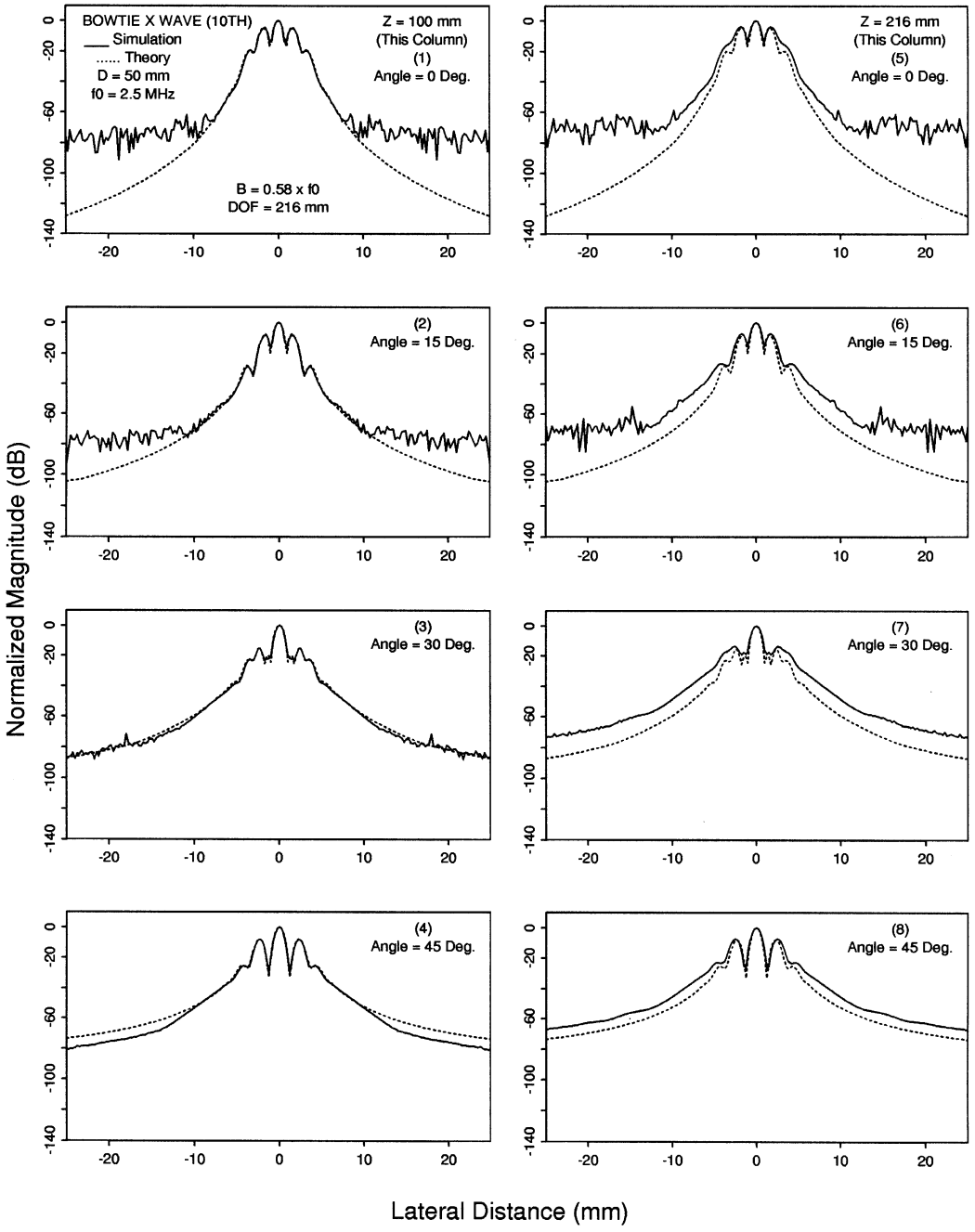

Fig. 5. This figure has the same format as that of Fig. 4 except that it is for the 10th derivative bowtie X wave. The parameters used in this figure are the same as those used in Figs. 2 and 3 of the theoretical beams and those in Fig. 4. The noise in the panels of the upper two rows is caused by the computation errors that exceed the extremely low sidelobes to be calculated.

Because any derivatives of the X waves in terms of the coordinate variables, x, y, z, or t, do not change the Axicon angle, ζ, the depth of field of the bowtie X waves is the same as that of the zeroth-order X wave when produced with the same aperture, D, and is also given by [31]

$$XZ_{max} = \frac{D}{2}\cot\zeta. \tag{27}$$

With the parameters used, the depth of field of the simulated bowtie X waves in Figs. 4 and 5 is about 216 mm. From Figs. 4 and 5, we see that the pulse-echo responses of the simulated bowtie X waves are very close to those of the theoretical waves except that near the boundary of the depth of field, $z = 216$ mm, sidelobes are increased. The noise shown in the first two rows ($\phi = 0°$ and $15°$) of Fig. 5 for the simulated 10th derivative bowtie X wave is caused by the computation errors that exceed the extremely low sidelobes of the wave to be calculated.

The simulated bowtie X waves in the $r-z$ planes are shown in Fig. 6. These waves are calculated with (19) and (20) and with the same parameters as those used in Fig. 1. They are

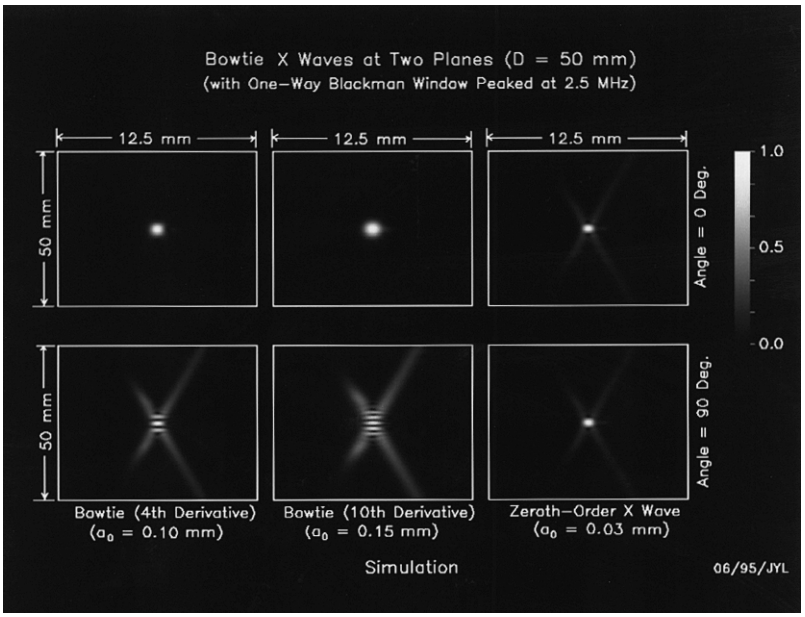

Fig. 6. One-way (transmission or reception only) 4th (panels in the left column) and 10th derivative (panels in the middle column) bowtie X waves shown in planes ($r - z$ planes) along the wave axis and calculated with the Rayleigh-Sommerfeld diffraction formula at the axial distance, $z = 100$ mm, and at two angles: $\phi = 0^\circ$ (panels in the upper row) and 90° (panels in the bottom row). The zeroth-order X wave (panels in the right column) is added for comparison. One-way Blackman window (13) is applied to all the images. The parameters used in this figure are the same as those in Fig. 1, except that the diameter of the radiator is 50 mm in the simulation. The gray-scale of the images in the panels is proportional to the analytic envelope of the real part of the waves. It is linear and normalized to the range from 0.0 to 1.0 in 256 levels.

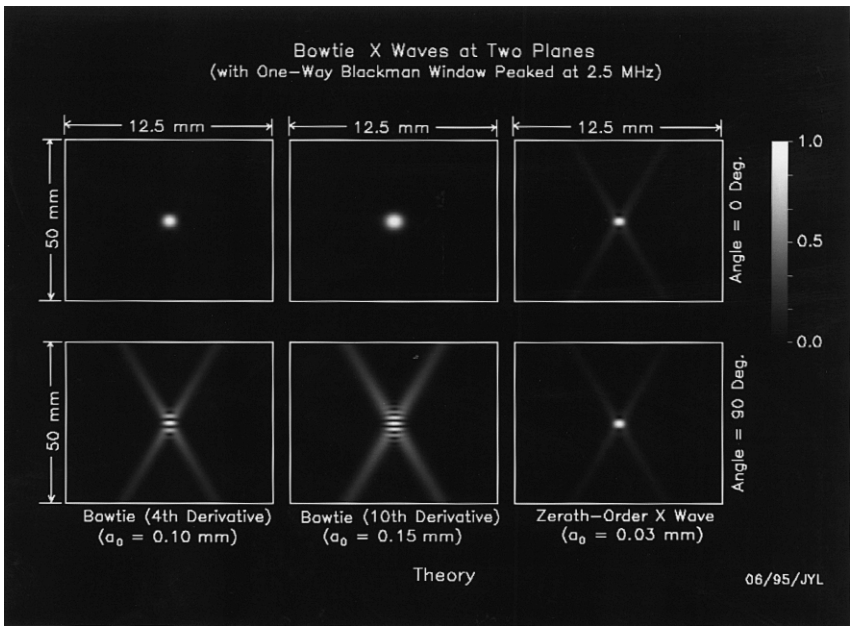

Fig. 7. This figure has the same format as Fig. 6, except that it is obtained analytically (see (10)–(12)). The parameters used in this figure are the same as those used in Fig. 1.

one-way fields (transmission fields or reception responses) and are produced with a radiator of 50-mm diameter. It is clear that the bowtie X waves have the same Axicon angle as the zeroth-order X wave.

Fig. 7 has the same format as Fig. 6 except that it is obtained from the theoretical bowtie X waves ((11) and (12)) and the zeroth-order X wave (10) filtered with the Blackman window function (13) and produced with an infinite aperture (Fig. 1). Comparing Figs. 6 and 7, one can see that they are very close. This means that the theoretical bowtie limited diffraction beams can be produced with a practical radiator of a finite aperture over a large depth of field.

C. Axial Field Responses

Line plots of the peak-to-peak values of the simulated one-way bowtie X waves versus the propagation distance, $z = c_1 t$, are shown in Fig. 8. The bowtie limited diffraction beams are

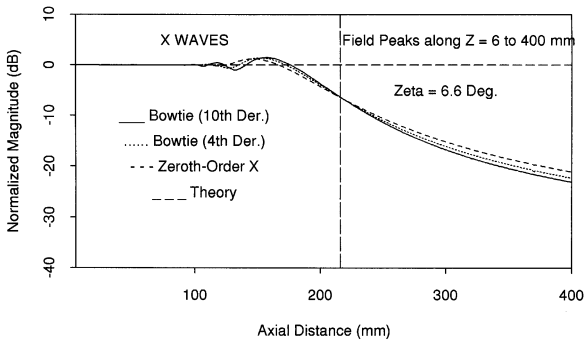

Fig. 8. Line plots of the peak-to-peak values of the real part of the one-way 4th (dotted line) and 10th derivative (full line) bowtie X waves and zeroth-order X wave (dashed line) versus the propagation distance, z, from 6 to 400 mm. The parameters of these beams are the same as those in Fig. 6. The line plot of the theoretical beams (long dashed line) is simply a straight horizontal line because they have an infinite depth of field. The vertical bar (very long dashed line) in the figure represents the depth of field (216 mm) of the simulated beams. The lateral axis is the propagation distance and the vertical axis represents the normalized magnitude from -40 dB to 10 dB.

produced with the same aperture and the Axicon angle and have the same depth of field as the zeroth-order X wave.

IV. Discussion

Bowtie limited diffraction beams (Fig. 1) and their application in pulse-echo systems for low-sidelobes and large depth of field imaging (Figs. 2 and 3) have been studied. Theoretically, these beams have an infinite depth of field. With practical radiators of finite aperture and bandwidth, these beams can be produced closely (Figs. 4–7) over a large depth of field (Fig. 8). In the following, the advantages and limitations of these new beams will be discussed.

A. Sidelobes

The bowtie limited diffraction beams studied in this paper have the advantages that they have very low sidelobes in the direction perpendicular to that of derivatives, and the sidelobes are even lower as the order of derivative increases (Fig. 1). Their asymptotic behaviors ((14) and (15)) in this direction are proportional to $1/r^{(m+1)/2}$, as $r \to \infty$, where m is the order of derivative and r is the radial distance. In the direction of derivatives, the asymptotic behaviors are the same as those of the original limited diffraction beams, i.e., are proportional to $1/r^{1/2}$. The asymptotic behaviors in other directions are between these two extreme cases. With these properties, bowtie limited diffraction beams can be applied to achieve both low-sidelobe and large depth of field in pulse-echo systems (transmit with a bowtie limited diffraction beam and receive with its 90° rotated response, see Figs. 2 and 3). For example, the sidelobes of the pulse-echo response of a 4th derivative bowtie limited diffraction beam are close to those of a linear or rectangular radiator in the focal plane (sinc function (18)), and the sidelobes of the pulse-echo response of a 10th derivative beam are comparable to those of a circular piston radiator in the focal plane (Jinc function (17)). In both cases, the sidelobes are much lower than those of the original limited diffraction beams (Figs. 2 and 3).

Sidelobes of the pulse-echo responses of the bowtie limited diffraction beams are angle dependent (Figs. 2 and 3). They are the lowest at $\phi = 0°$ and the highest at $\phi = 45°$.

B. Resolutions

Lateral resolution is usually measured with the -6-dB width of beams. With the same depth of field and aperture size, the lateral resolution of the pulse-echo responses of the bowtie limited diffraction beams increases as the central wavelength of the beams decreases. For a given central wavelength, the lateral resolution of the pulse-echo responses of the bowtie limited diffraction beams is comparable to those of the original limited diffraction beams (see Figs. 2 and 3) and increases with the order of derivative. However, the increase of resolution is at the expense of increased first sidelobes. Higher first sidelobes will increase the effective main beamwidth and thus reduce the effective lateral resolution. However, at some angles such as $\phi = 30°$ (Figs. 3–5), the first sidelobes are reduced. Therefore, we can rotate the pulse-echo responses of the bowtie limited diffraction beams so that the object to be imaged is scanned at these angles. The larger first sidelobes that are not in the scan direction can be treated as an increased slice thickness or a decreased out-of-plane resolution that does not have as strong an influence on image quality as the in-plane resolution.

C. Depth of Field

Given the same aperture size and the Axicon angle (for X waves) or scaling factor (for Bessel beams), the depth of field of bowtie limited diffraction beams of various orders is about the same as that of the original limited diffraction beams (Fig. 8) and can be calculated with the formulas of the original limited diffraction beams ((27) for X waves). For the theoretical bowtie limited diffraction beams, their depth of field is infinite because they are assumed to be produced with an infinite aperture (see the lateral straight line in Fig. 8).

The depth of field is a critical parameter for all limited diffraction beams. Within the depth of field, the simulated beams under the practical conditions are very close to the analytic beams (Figs. 4–7). At the depth of field (216 mm in our examples), the sidelobes of the simulated beams begin to increase (Figs. 4 and 5). Beyond the depth of field, these beams may diffract significantly.

D. Other New Limited Diffraction Beams

Bowtie limited diffraction beams studied in this paper are only one type of new limited diffraction beams. Numerous limited diffraction beams that might have practical applications are to be discovered. For example, taking derivatives of the zeroth-order limited diffraction beams in both x and y directions may result in a limited diffraction beam of a cross shape that could also be used for sidelobe reduction in pulse-echo systems (transmit with a cross beam and receive with its 45° rotated response). Taking derivatives of the higher-order limited diffraction beams ($n > 0$ in (4) and (5)) may result in other new beams.

E. Production of Bowtie Limited Diffraction Beams in Pulse-Echo Systems

One way to produce the pulse-echo responses of the bowtie limited diffraction beams is to use a 2-D array in both transmission and reception. To transmit the bowtie limited diffraction beams, the signals to drive the elements of the array can be weighted with the theoretical beams ((11) and (12)) evaluated at the surface of the radiator, $z = 0$. In reception, according to the principle of reciprocity, the signals from the elements can be weighted the same as in transmission to obtain a bowtie limited diffraction response. This method requires a large number of T/R switches because the number of elements of a 2-D array is usually very large in order to satisfy the Nyquist sampling rate of the aperture weighting functions. If the beams are steered with linear phase delays, the number of elements and thus the number of the T/R switches required may be even larger because the interelement distance in the direction of steering must be smaller than $\lambda/2$ [36], [37] to reduce the grating lobes, where λ is the wavelength.

The other way to produce the pulse-echo responses of the bowtie limited diffraction beams is also to use a 2-D array, but the array is divided into four quarters where the bowtie beam transmission uses two opposite quarters and the bowtie reception takes the other two. This method ignores the small weightings of the elements in the areas complementary to either the transmission or reception bowtie shape and thus is an approximation to the previous one. Its advantage is that no T/R switches are needed because of the separated transmission and reception. This also helps to remove the noise produced by the T/R switches. However, if a better approximation is desired, a small number of T/R switches are still needed for the elements around the center of the beams where the weighting functions have larger values.

For both methods, the electronic switches that rescale the weighting functions in the scan direction for compensating the loss of the effective aperture as the beam is steered off the axis by a linear phase delay are still required [36], [37]. However, in a steering range of ±45°, only a few switches are necessary to produce reasonably good beams [36]. If a mechanical scan is used, these switches can be removed because the effective aperture stays the same in the scan. The mechanical scan may also take the advantage of the symmetry of the beams and the low spatial frequency in some areas, such as those in larger radial distances, to reduce the number of elements. Fewer elements will not increase the grating lobes if the gaps between the elements are small [36].

In addition, because bowtie limited diffraction beams of higher-order derivatives have narrower (skinny) tie shapes, they could be produced with an 1.5-D array.

F. Possible Applications

Because the pulse-echo responses of the bowtie limited diffraction beams have low sidelobes and a large depth of field, they could have applications in medical imaging, tissue characterization, Doppler, underwater acoustics, nondestructive evaluation of materials (NDE), electromagnetics, radar, and optics.

G. Some Considerations

Bowtie limited diffraction beams are exact solutions of the wave equation (1) derived from the assumption that the media in which beams propagate are isotropic and homogeneous. Therefore, applications of these beams under conditions that are close to the assumption are expected to have the best results. If the conditions are far away from the assumption, the results may be compromised.

V. Conclusion

A new type of limited diffraction beams is developed. These beams are called bowtie limited diffraction beams because they have bowtie shapes in a plane perpendicular to the propagation axis of the beams. When these beams are applied to pulse-echo systems, their pulse-echo responses have very low sidelobes over a large depth of field, even if the beams are produced with a practical radiator that has a finite aperture and bandwidth. These new beams could have applications in medical imaging, tissue characterization, Doppler, underwater acoustics, nondestructive evaluation of materials (NDE), as well as other physics related areas such as electromagnetics and optics.

Appendix A

Asymptotic behaviors of the bowtie X waves in (11) and (12) as $r \to \infty$.

From the relationship between the polar and rectangular coordinates, we have

$$y = r \sin \phi, \tag{A1}$$

where ϕ is the angle in a plane perpendicular to the z-axis. For X waves, the slowest decay of the field occurs at the X branches [31, (21)]. For example, when $r = \frac{1}{\sin \zeta} \sqrt{(z \cos \zeta - ct)^2 - a_0^2}$ in (10), where $|z \cos \zeta - ct| \geq a_0$

$$|\Phi_{XBB_0}| = \left| a_0 / \sqrt{M} \right| \underset{r \to \infty}{\sim} 1/r^{1/2}, \tag{A2}$$

where "$\sim$" means "similar to."

With (A1) and (A2), the asymptotic behaviors of the bowtie X waves in (11) and (12) can be obtained

$$|\Phi_{X_{B4}}| \underset{r \to \infty}{\sim} b_1 \frac{\sin^4 \phi}{r^{1/2}} + b_2 \frac{\sin^2 \phi}{r^{3/2}} + d_1 \frac{1}{r^{5/2}} = \frac{b_1 \sin^4 \phi}{r^{1/2}} + O\left(\frac{1}{r^{1/2}}\right) \sin^2 \phi + \frac{d_1}{r^{(4+1)/2}}, \tag{A3}$$

and

$$|\Phi_{X_{B10}}| \underset{r \to \infty}{\sim} \frac{b_1 \sin^{10} \phi}{r^{1/2}} + \frac{b_2 \sin^8 \phi}{r^{3/2}} + \frac{b_3 \sin^6 \phi}{r^{5/2}} + \frac{b_4 \sin^4 \phi}{r^{7/2}} + \frac{b_5 \sin^2 \phi}{r^{9/2}} + \frac{d_1}{r^{11/2}} = \frac{b_1 \sin^{10} \phi}{r^{1/2}} + O\left(\frac{1}{r^{1/2}}\right) \sin^2 \phi + \frac{d_1}{r^{(10+1)/2}}, \tag{A4}$$

where "$O(\cdot)$" represents the terms that approach zero faster than the function inside the bracket as $r \to \infty$, b_i and d_i, $(i = 1, 2, \cdots)$, are a set of constants that may have different values for (A3) and (A4).

$$\frac{\partial^{10}}{\partial y^{10}}J(\alpha r)=$$
$$\Big[-\frac{92897280\alpha^2y^{10}}{r^{18}}+\frac{1290240\alpha^2y^8\big(180+7\alpha^2y^2\big)}{r^{16}}-\frac{201600\alpha^2y^6\big(1008+108\alpha^2y^2+\alpha^4y^4\big)}{r^{14}}$$
$$+\frac{1200\alpha^2y^4\big(60480+15120\alpha^2y^2+360\alpha^4y^4+\alpha^6y^6\big)}{r^{12}}$$
$$-\frac{\alpha^2y^2\big(9072000+6048000\alpha^2y^2+302400\alpha^4y^4+1800\alpha^6y^6+\alpha^8y^8\big)}{r^{10}}$$
$$+\frac{630\alpha^2\big(288+1080\alpha^2y^2+120\alpha^4y^4+\alpha^6y^6\big)}{r^8}-\frac{945\alpha^4\big(12+5\alpha^2y^2\big)}{r^6}\Big]J_0(\alpha r)$$
$$+\Big[\frac{185794560\alpha y^{10}}{r^{19}}-\frac{10321920\alpha y^8\big(45+4\alpha^2y^2\big)}{r^{17}}+\frac{1693440\alpha y^6\big(240+60\alpha^2y^2+\alpha^4y^4\big)}{r^{15}}$$
$$-\frac{9600\alpha y^4\big(15120+9072\alpha^2y^2+405\alpha^4y^4+2\alpha^6y^6\big)}{r^{13}}$$
$$+\frac{50\alpha y^2\big(362880+604800\alpha^2y^2+60480\alpha^4y^4+720\alpha^6y^6+\alpha^8y^8\big)}{r^{11}}$$
$$-\frac{45\alpha\big(8064+80640\alpha^2y^2+20160\alpha^4y^4+448\alpha^6y^6+\alpha^8y^8\big)}{r^9}+\frac{630\alpha^3\big(108+135\alpha^2y^2+5\alpha^4y^4\big)}{r^7}-\frac{945\alpha^5}{r^5}\Big]J_1(\alpha r)\,. \tag{B4}$$

APPENDIX B

The derivatives in (25),

$$\frac{\partial^m}{\partial y^m}J_0\Big(\frac{\omega}{c}r\sin\zeta\Big), \tag{B1}$$

for $m=4$ and 10, respectively, and their relationship with the bowtie Bessel beams (see (3) and (5)).

For a given frequency or a constant ω, if $\alpha=\frac{\omega}{c}\sin\zeta$, (B1) becomes

$$\frac{\partial^m}{\partial y^m}J_0(\alpha r)\,. \tag{B2}$$

From (3) and (5), one sees that (B2) is an mth-derivative bowtie Bessel beam with $n=0$, evaluated at $z=c_1t$, where $c_1=\omega/\beta$ is the phase velocity.

For $m=4$ and 10, we obtain

$$\frac{\partial^4}{\partial y^4}J_0(\alpha r)=$$
$$\left[-\frac{24\alpha^2y^4}{r^6}+\frac{\alpha^2y^2\big(24+\alpha^2y^2\big)}{r^4}-\frac{3\alpha^2}{r^2}\right]J_0(\alpha r)$$
$$+\left[\frac{48\alpha y^4}{r^7}-\frac{8\alpha y^2\big(6+\alpha^2y^2\big)}{r^5}+\frac{6\alpha\big(1+\alpha^2y^2\big)}{r^3}\right]J_1(\alpha r) \tag{B3}$$

and (B4), respectively, shown at the top of the page.

Similar to the bowtie X waves in (11) and (12), the constants that normalize the peaks of the bowtie Bessel beams in (B3) and (B4) to one can be obtained and are given by $a_{J_{B4}}=8/\big(3\alpha^4\big)$ and $a_{J_{B10}}=-256/\big(63\alpha^{10}\big)$, respectively.

To show the properties of the bowtie Bessel beams, we need to know the asymptotic behaviors of (B3) and (B4). With the formula $|J_n(\alpha r)|\underset{r\to\infty}{\sim}1/r^{1/2}$ [60, p. 622], we obtain the results that are similar to those of the bowtie X waves in Appendix A

$$\left|\frac{\partial^4}{\partial y^4}J(\alpha r)\right|\underset{r\to\infty}{\sim}\frac{b_1\sin^4\phi}{r^{1/2}}+\frac{\sin^2\phi\big(b_2+b_3\sin^2\phi\big)}{r^{3/2}}$$
$$+\frac{\sin^2\phi\big(b_4+b_5\sin^2\phi\big)}{r^{5/2}}+\frac{\sin^2\phi\big(b_6+b_7\sin^2\phi\big)}{r^{7/2}}$$
$$+\frac{d_1}{r^{5/2}}+\frac{d_2}{r^{7/2}}=\frac{b_1\sin^4\phi}{r^{1/2}}+O\left(\frac{1}{r^{1/2}}\right)\sin^2\phi$$
$$+\frac{d_1}{r^{(4+1)/2}}+O\left(\frac{1}{r^{(4+1)/2}}\right) \tag{B5}$$

and

$$\left|\frac{\partial^{10}}{\partial y^{10}}J(\alpha r)\right|\underset{r\to\infty}{\sim}\frac{b_1\sin^{10}\phi}{r^{1/2}}+\frac{\sin^8\phi\big(b_2+b_3\sin^2\phi\big)}{r^{3/2}}$$
$$+\frac{\sin^6\phi\big(b_4+b_5\sin^2\phi+b_6\sin^4\phi\big)}{r^{5/2}}$$
$$+\frac{\sin^4\phi\big(b_7+b_8\sin^2\phi+b_9\sin^4\phi+b_{10}\sin^6\phi\big)}{r^{7/2}}$$
$$+\frac{\sin^2\phi\big(b_{11}+b_{12}\sin^2\phi+b_{13}\sin^4\phi+b_{14}\sin^6\phi+b_{15}\sin^8\phi\big)}{r^{9/2}}$$
$$+\frac{\sin^2\phi\big(b_{16}+b_{17}\sin^2\phi+b_{18}\sin^4\phi+b_{19}\sin^6\phi+b_{20}\sin^8\phi\big)}{r^{11/2}}$$
$$+\frac{\sin^2\phi\big(b_{21}+b_{22}\sin^2\phi+b_{23}\sin^4\phi+b_{24}\sin^6\phi+b_{25}\sin^8\phi\big)}{r^{13/2}}$$
$$+\frac{\sin^2\phi\big(b_{26}+b_{27}\sin^2\phi+b_{28}\sin^4\phi+b_{29}\sin^6\phi+b_{30}\sin^8\phi\big)}{r^{15/2}}$$
$$+\frac{\sin^2\phi\big(b_{31}+b_{32}\sin^2\phi+b_{33}\sin^4\phi+b_{34}\sin^6\phi+b_{35}\sin^8\phi\big)}{r^{17/2}}$$
$$+\frac{\sin^2\phi\big(b_{36}+b_{37}\sin^2\phi+b_{38}\sin^4\phi+b_{39}\sin^6\phi+b_{40}\sin^8\phi\big)}{r^{19/2}}$$

$$+\frac{d_1}{r^{11/2}}+\frac{d_2}{r^{13/2}}+\frac{d_3}{r^{15/2}}+\frac{d_4}{r^{17/2}}+\frac{d_5}{r^{19/2}}$$
$$=\frac{b_1\sin^{10}\phi}{r^{1/2}}+O\left(\frac{1}{r^{1/2}}\right)\sin^2\phi+\frac{d_1}{r^{(10+1)/2}}+O\left(\frac{1}{r^{(10+1)/2}}\right). \quad \text{(B6)}$$

ACKNOWLEDGMENT

The author thanks Dr. Greenleaf in the Biodynamics Research Unit, Mayo Clinic for reviewing the manuscript. The author also thanks E. C. Quarve for secretarial assistance.

REFERENCES

[1] J. N. Brittingham, "Focus wave modes in homogeneous Maxwell's equations: transverse electric mode," *J. Appl. Phys.*, vol. 54, no. 3, pp. 1179–1189, 1983.
[2] R. W. Ziolkowski, "Exact solutions of the wave equation with complex source locations," *J. Math. Phys.*, vol. 26, no. 4, pp. 861–863, Apr. 1985.
[3] R. W. Ziolkowski, D. K. Lewis, and B. D. Cook, "Evidence of localized wave transmission," *Phys. Rev. Lett.*, vol. 62, no. 2, pp. 147–150, Jan. 9, 1989.
[4] A. M. Shaarawi, I. M. Besieris, and R. W. Ziolkowski, "Localized energy pulse train launched from an open, semi-infinite, circular waveguide," *J. Appl. Phys.*, vol. 65, no. 2, pp. 805–813, 1989.
[5] I. M. Besieris, A. M. Shaarawi, and R. W. Ziolkowski, "A bidirectional traveling plane wave representation of exact solutions of the scalar wave equation," *J. Math. Phys.*, vol. 30, no. 6, pp. 1254–1269, 1989.
[6] E. Heyman, B. Z. Steinberg, and L. B. Felsen, "Spectral analysis of focus wave modes," *J. Opt. Soc. Amer. A*, vol. 4, no. 11, pp. 2081–2091, Nov. 1987.
[7] R. W. Ziolkowski, "Localized transmission of electromagnetic energy," *Phys. Rev. A.*, vol. 39, no. 4, pp. 2005–2033, Feb. 15, 1989.
[8] J. V. Candy, R. W. Ziolkowski, and D. K. Lewis, "Transient waves: Reconstruction and processing," *J. Acoust. Soc. Amer.*, vol. 88, no. 5, pp. 2248–2258, Nov. 1990.
[9] ———, "Transient wave estimation: A multichannel deconvolution application," *J. Acoust. Soc. Amer.*, vol. 88, no. 5, pp. 2235–2247, Nov. 1990.
[10] R. W. Ziolkowski and D. K. Lewis, "Verification of the localized wave transmission effect," *J. Appl. Phys.*, vol. 68, no. 12, pp. 6083–6086, Dec. 15, 1990.
[11] J. Durnin, "Exact solutions for nondiffracting beams. I. The scalar theory," *J. Opt. Soc. Amer. A*, vol. 4, no. 4, pp. 651–654, 1987.
[12] J. Durnin, J. J. Miceli, Jr., and J. H. Eberly, "Diffraction-free beams," *Phys. Rev. Lett.*, vol. 58, no. 15, pp. 1499–1501, Apr. 13, 1987.
[13] J. Lu, H. Zou, and J. F. Greenleaf, "Biomedical ultrasound beam forming," *Ultrasound Med. Biol.*, vol. 20, no. 5, pp. 403–428, July 1994.
[14] J. Lu and J. F. Greenleaf, "Sidelobe reduction for limited diffraction pulse-echo systems," *IEEE Trans. Ultrason., Ferroelec., Freq. Contr.*, vol. 40, no. 6, pp. 735–746, Nov. 1993.
[15] G. Indebetow, "Nondiffracting optical fields: Some remarks on their analysis and synthesis," *J. Opt. Soc. Amer. A*, vol. 6, no. 1, pp. 150–152, Jan. 1989.
[16] K. Uehara and H. Kikuchi, "Generation of near diffraction-free laser beams," *Appl. Phys. B*, vol. 48, pp. 125–129, 1989.
[17] L. Vicari, "Truncation of nondiffracting beams," *Optics Commun.*, vol. 70, no. 4, pp. 263–266, Mar. 15, 1989.
[18] D. K. Hsu, F. J. Margetan, and D. O. Thompson, "Bessel beam ultrasonic transducer: Fabrication method and experimental results," *Appl. Phys. Lett.*, vol. 55, no. 20, pp. 2066–2068, Nov. 13, 1989.
[19] J. A. Campbell and S. Soloway, "Generation of a nondiffracting beam with frequency independent beam width," *J. Acoust. Soc. Amer.*, vol. 88, no. 5, pp. 2467–2477, Nov. 1990.
[20] J. Lu and J. F. Greenleaf, "Effect on J_0 nondiffracting beam of deleting central elements of J_0 annular array transducer," *Ultrason. Imag.,* vol. 13, no. 2, p. 203, Apr. 1991 (abs.).
[21] J. Lu, T. K. Song, R. R. Kinnick, and J. F. Greenleaf, "*In vitro* and *in vivo* real-time imaging with ultrasonic limited diffraction beams," *IEEE Trans. Med. Imag.,* vol. 12, no. 4, pp. 819–829, Dec. 1993.
[22] J. Lu and J. F. Greenleaf, "Diffraction-limited beams and their applications for ultrasonic imaging and tissue characterization," in *New Developments in Ultrasonic Transducers and Transducer Systems,* F. L. Lizzi, Ed., *Proceedings SPIE*, vol. 1733, pp. 92–119, 1992.
[23] ———, "Pulse-echo imaging using a nondiffracting beam transducer," *Ultrasound Med. Biol.,* vol. 17, no. 3, pp. 265–281, May 1991.
[24] ———, "Ultrasonic nondiffracting transducer for medical imaging," *IEEE Trans. Ultrason., Ferroelec., Freq. Contr.,* vol. 37, no. 5, pp. 438–447, Sept. 1990.
[25] ———, "Evaluation of a nondiffracting transducer for tissue characterization," in *IEEE 1990 Ultrason. Symp. Proc.,* 90CH2938–9, vol. 2, pp. 795–798, 1990.
[26] ———, "Producing deep depth of field and depth-independent resolution in NDE with limited diffraction beams," *Ultrason. Imag.,* vol. 15, no. 2, pp. 134–149, Apr. 1993.
[27] J. Lu, X.-L. Xu, H. Zou, and J. F. Greenleaf, "Application of Bessel beam for Doppler velocity estimation," *IEEE Trans. Ultrason., Ferroelec., Freq. Contr.*, vol. 42, no. 4, pp. 649–662, July 1995.
[28] J. Ojeda-Castaneda and A. Noyola-lglesias, "Nondiffracting wavefields in grin and free-space," *Microwave Optical Technol. Lett.*, vol. 3, no. 12, pp. 430–433, Dec. 1990.
[29] R. Donnelly, D. Power, G. Templeman, and A. Whalen, "Graphic simulation of superluminal acoustic localized wave pulses," *IEEE Trans. Ultrason., Ferroelec., Freq. Contr.,* vol. 41, no. 1, pp. 7–12, 1994.
[30] R. Donnelly and R. W. Ziolkowski, "Designing localized waves," *Proc. Royal Soc. Lond., A*, vol. 440, pp. 541–565, 1993.
[31] J. Lu and J. F. Greenleaf, "Nondiffracting X waves—Exact solutions to free-space scalar wave equation and their finite aperture realizations," *IEEE Trans. Ultrason., Ferroelec., Freq. Contr.,* vol. 39, no. 1, pp. 19–31, Jan. 1992.
[32] ———, "Experimental verification of nondiffracting X waves," *IEEE Trans. Ultrason., Ferroelec., Freq. Contr.,* vol. 39, no. 3, pp. 441–446, May 1992.
[33] ———, "Theory and acoustic experiments of nondiffracting X waves," in *IEEE 1991 Ultrason. Symp. Proc.,* 91CH3079–1, vol. 2, pp. 1155–1159, 1991.
[34] J. Lu, H.-H. Zou, and J. F. Greenleaf, "A new approach to obtain limited diffraction beams," *IEEE Trans. Ultrason., Ferroelec., Freq. Contr.*, vol. 42, no. 5, pp. 850–853, Sept. 1995.
[35] T. K. Song, J. Lu, and J. F. Greenleaf, "Modified X waves with improved field properties," *Ultrason. Imag.,* vol. 15, no. 1, pp. 36–47, Jan. 1993.
[36] J. Lu and J. F. Greenleaf, "A study of two-dimensional array transducers for limited diffraction beams," *IEEE Trans. Ultrason., Ferroelec., Freq. Contr.,* vol. 41, no. 5, pp. 724–739, Sept. 1994.
[37] ———, "Steering of limited diffraction beams with a two-dimensional array transducer," in *IEEE 1992 Ultrason. Symp. Proc.,* 92CH3118–7, vol. 1, pp. 603–607, 1992.
[38] ———, "Formation and propagation of limited diffraction beams," *Acoust. Imag.,* Y. Wei and B.-L. Gu, Eds., vol. 20, pp. 331–343, 1993.
[39] M. Fatemi and M. A. Arad, "A novel imaging system based on nondiffracting X waves," in *IEEE 1992 Ultrason. Symp. Proc.*, 92CH3118–7, vol. 1, pp. 609–612, 1992.
[40] J. Lu and J. F. Greenleaf, "Comparison of sidelobes of limited diffraction beams and localized waves," *Acoust. Imag.,* J. P. Jones, Ed., vol. 21 (to be published in 1995).
[41] ———, "Simulation of imaging contrast of nondiffracting beam transducer," *J. Ultrasound Med.,* vol. 10, no. 3 (suppl.), p. S4, Mar. 1991 (abs.).
[42] ———, "Experiment of imaging contrast of J_0 Bessel nondiffracting beam transducer," *J. Ultrasound Med.,* vol. 11, no. 3 (suppl.), p. S43, Mar. 1992 (abs.).
[43] J. P. Wild, "A new method of image formation with annular apertures and application in radio astronomy," in *Proc. Royal Soc. A,* vol. 286, pp. 499–509, 1965.
[44] C. B. Burckhardt, P. A. Grandchamp, and H. Hoffmann, "Methods for increasing the lateral resolution of B-scan," *Acoustic Holography,* P. S. Green, Ed., vol. 5, pp. 391–413, 1973.
[45] D. Vilkomerson, "Acoustic imaging with thin annular apertures," *Acoustic Holography,* P. S. Green, Ed., vol. 5, pp. 283–316, 1973.
[46] J. H. McLeod, "The Axicon: A new type of optical element," *J. Opt. Soc. Amer.*, vol. 44, no. 8, pp. 592–597, Aug. 1954.
[47] C. B. Burckhardt, H. Hoffmann, and P. A. Grandchamp, "Ultrasound axicon: A device for focusing over a large depth," *J. Acoust. Soc. Amer.*, vol. 54, no. 6, pp. 1628–1630, Dec. 1973.
[48] F. S. Foster, M. S. Patterson, M. Arditi, and J. W. Hunt, "The conical scanner: A two transducer ultrasound scatter imaging technique," *Ultrason. Imag.,* vol. 3, no. 1, pp. 62–82, Apr. 1981.

[49] C. B. Burckhardt, P. A. Grandchamp, and H. Hoffmann, "Focusing ultrasound over a large depth with an annular transducer—An alternative method," *IEEE Trans. Sonics Ultrason.*, vol. SU-22, no. 1, pp. 11–15, Jan. 1975.
[50] A. Macovski and S. J. Norton, "High-resolution B-scan systems using a circular array," *Acoustic Holography,* N. Booth, Ed., vol. 6, pp. 121–143, 1975.
[51] M. Moshfeghi, "Sidelobe suppression in annular array and axicon imaging systems," *J. Acoust. Soc. Amer.*, vol. 83, no. 6, pp. 2202–2209, June 1988.
[52] J. Lu and J. F. Greenleaf, "A study of sidelobe reduction for limited diffraction beams," in *IEEE 1993 Ultrason. Symp. Proc.*, 93CH3301–9, vol. 2, pp. 1077–1082, 1993.
[53] M. S. Patterson, F. S. Foster, and D. Lee, "Sidelobe and speckle reduction for an eight sector conical scanner," in *IEEE 1981 Ultrason. Symp. Proc.*, 81CH1689–9, vol. 2, pp. 632–637, 1981.
[54] J. Lu and J. F. Greenleaf, "Sidelobe reduction of nondiffracting pulse-echo images by deconvolution," *Ultrason. Imag.,* vol. 14, no. 2, p. 203, Apr. 1992 (abs.).
[55] S. W. Smith and O. T. von Ramm, "The Maltese cross processor: Speckle reduction for circular transducers," *Ultrason. Imag.,* vol. 10, no. 3, pp. 153–170, July 1988.
[56] M. S. Patterson and F. S. Foster, "Acoustic fields of conical radiators," *IEEE Trans. Sonics Ultrason.*, vol. SU-29, no. 2, pp. 83–92, Mar. 1982.
[57] A. V. Oppenheim and R. W. Schafer, *Digital Signal Processing*. Englewood Cliffs, NJ: Prentice-Hall, 1975, ch. 5.
[58] J. W. Goodman, *Introduction to Fourier Optics.* New York: McGraw-Hill, 1968, ch. 2–4.
[59] R. Bracewell, *The Fourier Transform and its Applications*. New York: McGraw-Hill, 1965, ch. 4 and 6.
[60] P. M. Morse and H. Feshbach, *Methods of Theoretical Physics, Part I*. New York: McGraw-Hill, 1953, ch. 4–7.

Jian-yu Lu (M'88), for photograph and biography, see p. 661 of the July 1995 issue of this TRANSACTIONS.